

Title: Imaging the controllable rotation of a skyrmion crystal driven by femtosecond laser pulses

Authors: Phoebe Tengdin^{1*†}, Benoît Truc^{1†}, Alexey Sapozhnik^{1†}, Simone Gargiulo¹, Ivan Madan¹, Thomas Schoenenberger², Priya R. Baral³, Ping Che⁴, Arnaud Magrez³, Dirk Grundler⁴, Henrik M. Rønnow², Thomas Lagrange¹, Fabrizio Carbone¹

*phoebe.tengdin@epfl.ch

†these authors contributed equally

Affiliations :

¹Institute of Physics, LUMES, École Polytechnique Fédérale de Lausanne (EPFL), Lausanne, Switzerland

²Institute of Physics, LQM, École Polytechnique Fédérale de Lausanne (EPFL), Lausanne, Switzerland

³Institute of Physics, Crystal Growth Facility, Ecole Polytechnique Fédérale de Lausanne (EPFL), Lausanne, Switzerland

⁴Institute of Materials (IMX), Laboratory of Nanoscale Magnetic Materials and Magnonics, Ecole Polytechnique Fédérale de Lausanne (EPFL), Lausanne, Switzerland

Abstract: Control of topological magnetic textures has attracted intense interest due to the potential applications for these structures in spintronic devices. Recent advances in electron microscopy have enabled imaging of individual skyrmions, however the full understanding of their ultrafast dynamics has remained inaccessible. Here we show via *cryo*- Lorentz microscopy that a single circularly polarized femtosecond laser pulse can induce controlled rotation of a skyrmion crystal. Pulses of light with an energy below the bandgap of the Mott insulator Cu₂OSeO₃ drive spin currents whose direction and strength determine the direction and degree of the skyrmion crystal rotation. Thermodynamic calculations confirm that the rotation dynamics triggered take place on a timescale more than six orders of magnitude faster than previously measured. This direct manipulation of topological order via laser pulses can be used to engineer spin-based logical devices on much faster timescales than available methods.

MAIN TEXT:

Introduction:

Skyrmions hold promise as a means of logical operations in spin based devices due to their small size, sensitivity to manipulation by weak electrical and spin currents, and topological stability[1]. When an electron traverses a skyrmion's magnetic structure, the topological ordering causes the electron's spin to pick up a Berry phase. This causes a Lorentz force on the electron and also results in a net force on skyrmions oriented perpendicular to the flow of electric current, known as the Skyrmion Hall effect [2], [3]. The effect provides a greatly enhanced coupling of electrical current to the magnetic texture, five orders of magnitude more efficient than for current driven manipulation of domain walls[4], [5]. In analogy to the case of electrical current, skyrmions present in an insulating host material will be subject to similar forces when exposed to a pure spin current[6]. However, this process can proceed without the Ohmic losses that exist when using electrical current. Additionally, excitation of spin currents can be achieved in an ultrafast and contact free manner using ultrafast lasers on femtosecond timescales[7], [8].

Experiments using femtosecond lasers to excite ferromagnetic materials have shown that these light pulses can generate spin currents that have pulse widths in the fs timescale and can travel up to ballistic speeds [9]–[13]. Circularly polarized pulses can also induce a magnetization in the material and drive switching of the magnetic order via the inverse Faraday effect [14]. However, the microscopic details about the magnitude and direction of the propagation of spin current on ultrafast timescales is not fully understood. Experiments investigating these spin currents have been ultimately constrained by a limited ability to directly image spin on the relevant length (nanometer) and time (femtosecond) scales.

The emergence of Cu_2OSeO_3 as a skyrmion hosting Mott insulating material with multiferroic properties and bulk Dzyaloshinskii-Moriya Interaction (DMI) opens the possibility to study and manipulate topological order and skyrmion dynamics in the absence of electric currents, purely under the influence of spin currents or electric field. Additionally, spin currents in Cu_2OSeO_3 have been shown to have an exceptionally low damping and correspondingly long mean free path, making them effective candidates as a means to manipulate spin order[15], [16]. Recent works have demonstrated the ability to rotate the skyrmion crystal in Cu_2OSeO_3 via spin current[17], [18], electric fields[19], [20], and a magnetic field gradient in doped crystals[21]. In [17], [18], the spin currents were induced with a strong local heat gradient generated from a high power electron beam. For all previous experiments of this kind, the rotation proceeded on the timescale of milliseconds to seconds, more than six orders of magnitude slower than the timescales typically possible using femtosecond lasers as used here.

In this work, we take advantage of the strong coupling between topological ordering and spin currents in Cu_2OSeO_3 to drive skyrmion rotational motion with single femtosecond pulses of circularly polarized near-infrared light. After each individual laser pulse, we image the skyrmion crystal in real space via *in-situ* cryo-Lorentz force transmission electron microscopy (L-TEM). We show that with each laser pulse we rotate the skyrmion crystal by a controlled amount. The amount and direction of rotation depend sensitively upon the polarization and fluence of the pulse and the direction of the propagation of the spin current in the material. Through analysis of our images we generate a detailed mapping of the rotations present with a precision that is only limited by the natural length scale of the skyrmions themselves ($\sim 60\text{nm}$). Using finite element simulations, we show that all heat has left the sample within $1.3\ \mu\text{s}$, indicating that the rotations are completed within $1.3\ \mu\text{s}$ following the laser pulse excitation.

Thus our work advances previously reported rates of rotation by over six orders of magnitude[17]. Additionally, the energy of the light used for excitation, at 1 eV, is far beneath the bandgap of the skyrmion host material, and thus control of the material is achieved with remarkably low values of absorbed fluence, potentially enabling future ultrafast and highly efficient devices.

Results:

In Figure 1a and b we show real space cryo-LTEM under-focused images of the skyrmion crystal in Cu_2OSeO_3 discussed in this work. Figure 1a shows a metastable skyrmion crystal that has formed when we cool the thin lamella from above the Curie temperature ($\sim 60\text{K}$) to 5K under an applied magnetic field of 34mT. Next we irradiate the sample with individual femtosecond laser pulses, and observe that the skyrmion crystal rotates as shown in Figure 1b. The microscopic physics responsible for the rotation process is shown in Figure 1c. Excitation by a near infrared femtosecond laser pulse generates spin currents that flow in an inward direction from the sides of the material. The Gaussian profile of the laser beam has a FWHM of 40 μm , providing a nearly uniform illumination for our sample (with a dimension of 10 μm). Spin currents can be excited from an inhomogeneity, in our case from the edges of our lamella. Additionally, there exists a unidirectional temperature gradient due to our sample's geometry and thermal anchoring. The combination of the spin currents generated by the laser pulse with the cooling temperature gradient provides a Magnus force acting on the skyrmions which results in rotation of the skyrmions in different senses (clockwise or counterclockwise) from different regions of the sample. Further details on this process are found in Ref [22].

Figure 2a illustrates our procedure for tracking the rotation of the skyrmion crystal in the real space TEM images. After each successive laser pulse, we take an image and then take the

Fourier transform (FT) of the real-space image (or a subsection of an image) and calculate the angle of the FT in a polar coordinate system. We repeat this process, allowing us to map the change in the angle of the skyrmion crystal following a train of pulses of near-infrared radiation. Further details about the pulse train and imaging settings are given in the Methods section. In Figure 2b, we extract and plot the angle of a single peak in the FT of the skyrmion crystal while illuminating the sample with a pulse train of either circularly or linearly polarized light. For the circularly polarized light, each pulse rotates the skyrmion crystal by a discrete amount, while the linearly polarized light does not rotate the skyrmion crystal. This difference between the two polarizations suggests that the circularly polarized pulse drives excitation of magnons (the quanta of spin current) by the inverse Faraday effect [23].

In Figure 3 we use this technique to map the rotation of the skyrmion crystal in real space while again illuminating the sample with a train of femtosecond NIR laser pulses. We divide the real space image of Figure 3a into 100 individual boxes, for each of which we take the FT of the (sub)image and then plot the region around a single point in the FT. In Figures 3b-d we show cutouts of the rotation present in different regions of the sample. Note that the rotation proceeds in a different direction on different sides of the lamella. We use this information to generate Figure 4a where we have displayed the rotation present in each subregion of a 10x10 grid of the sample. In each box we mark the direction of rotation by the color.

We model the thermodynamics of the sample following ultrafast laser excitation using the finite element method (See SI for further details). Our model uses experimental values for the heat capacity and heat conduction in Cu_2OSeO_3 [15], [24]. According to this simulation, the primary thermal gradient that cools the sample is along the direction of the cold finger thermostat, or in an up-down direction in Fig.1c. This gradient coupled with the spin currents

generated by excitation of the femtosecond laser pulse can explain the rotation of the skyrmion crystal observed in our real space images. Regions propagating clockwise correspond to spin current propagating in the same direction as the (hot to cold) temperature gradient, while regions rotating in the counterclockwise direction correspond to spin current propagating in the opposite direction. On the left and right side of the image, the current propagates perpendicular to the cooling gradient, causing either clockwise or counterclockwise rotation as also shown in ref [22]. The rate of the rotation corresponds to the strength of the spin current. In the center of the image, the direction and magnitude of the vectors flip.

For the image shown in Figure 3a, our field of view was centered in the middle of the sample, thus we expect that this change in the magnitude and direction of the rotation of the skyrmion clusters is due to a change in the direction of the spin currents generated by the laser pulse. Additionally, the rotation rate is greater on the upper half of the picture than it is on the lower half. This makes sense because the temperature gradient in the presence of a magnetization also generates spin currents due to the Spin Seebeck effect [25]. These currents add to the currents in the upper part of the image, while they subtract from the current in the lower part of the image. Images taken from regions of the sample close to the edges show unidirectional rotation dynamics, confirming our hypothesis that the spin currents are generated from the edges and propagate into the center of the lamella (see SI for these data taken from other regions of the lamella).

To understand the timescales relevant for this rotation process, it is important to identify the evolution of temperature in the sample following the absorption of the laser pulse. Our calculations show that the sample reaches a maximum temperature of $\sim 49\text{K}$ and remains at that temperature for at least 1-2 ns. Afterwards, cooling via the heatsink proceeds and there is a

unidirectional thermal gradient of approximately 44K across the lamella from 10 ns until several hundred ns, and finally all cooling is completed within 1.3 μ s. After the sample cools completely and the spin currents are damped, the skyrmion crystal remains in the same rotated configuration until the next pulse arrives. The peak temperature of 49K reached in the film is below the paramagnetic melting point of the skyrmion crystal, thus the sample can still “remember” the previous skyrmion orientation, which explains well the rotation observed in our images. This is a fundamentally different mechanism than many previous studies of skyrmion or magnetic bubble formation[26], [27]. We note that in this experiment, the electron beam plays a negligible role in heating the lamella. We never observe any rotation from the skyrmion crystal under these imaging conditions (temperature, field) without external excitation. See SI for detailed calculations of the (negligible) heating from the electron beam.

Real space imaging via cryo-Lorentz force microscopy allows us to directly observe the rotation of the skyrmion crystal following each successive laser pulse. We found that by analyzing sub regions of the sample, we could better isolate the different regions of the skyrmion rotation. For the data presented in Figures 3 and 4, the grid size that led to the best isolation of clockwise and counterclockwise rotation regions corresponded to an analysis subregion of 460 nm, taken near the center of the sample. Since the skyrmion crystal period in this material is approximately 60 nm, this corresponds to a cluster of 7-8 skyrmions across, or approximately 50 skyrmions. Skyrmions in Cu_2OSeO_3 have Lennard-Jones type long range attractive forces between them and previous work has shown that they typically form clusters of this size in a helical background, making them likely to move and also rotate in clusters of approximately this size [28], [29].

Additionally, we observe that the magnitude of rotation depends sensitively on the amount of laser fluence used in the experiment. This dependence is shown in Figure 4b. We observed a threshold value needed to rotate the skyrmion crystal at 0.04 mJ/cm^2 , after which rotation proceeds at the same rate until reaching the threshold of 0.09 mJ/cm^2 , and increases at larger rates for higher fluences.

Discussion:

Notably, excitation at 1 eV in Cu_2OSeO_3 takes place at extremely low levels of absorbed fluence[30]. Previous studies using circularly polarized light at this energy with comparable fluences showed that this light excites collective magnetic excitations (magnons) in Cu_2OSeO_3 via the inverse Faraday effect [23]. These excitations have a lifetime of a few ns, persisting even longer when the temperature of the material is lowered. On this timescale, the excitations can have a lifetime comparable to the thermal gradient which occurs due to cooling the lamella via the cryostat. Together these forces drive the rotational motion observed in the crystal. In the study of Ogawa et. al. [23], the measured excitation was only measured in a bulk crystal, where an average was taken over the entire size of the probe beam (with a FWHM of about 100um), thus individual skyrmion motions were not resolved.

Generation and manipulation of sub-ps spin currents is a critical element for enabling ultrafast spintronic devices, thus techniques for imaging spin currents with high spatial and temporal resolution are urgently needed. By coupling spin currents to the Berry curvature of our skyrmionic structures, we provide a real-space mapping of the relative magnitude and direction of the currents in our material following femtosecond laser pulsed irradiation. This technique is moreover only limited in spatial resolution by the natural cluster scale of skyrmions in the material, which in some materials could be as low as 10s of nanometers [31]. On this scale our

resolution of the spin current could be comparable to studies of spin current conducted using synchrotron-based scanning transmission x-ray microscopy (STXM), without the need for the use of large scale facilities[32], and with the ability to record the unique distribution of spin current generated by femtosecond laser pulses. In this way our technique could be a powerful tool to understand the propagation of spin current in multilayer structures and guide the development of next generation spintronic devices.

In this experiment, the direction and magnitude of the coupling to the topology (i.e. rotation dynamics) can be controlled via tailoring the characteristics of the laser beam. We show that fluence and polarization can both directly control the rotation, while other parameters such as the beam shape have not yet been explored. To modify the spin currents and operate spin-based devices, we could imagine using spatially varied laser beam profiles such as Laguerre-Gaussian beams to generate tailored device frameworks as needed for logical operations. Tightly focusing these beams may also offer the possibility to generate individual skyrmions, as shown in ref. [33], while the orbital angular momentum in the beams may lead to an increased inverse Faraday effect, driving even more efficient rotations[34]. Thus, our work offers the possibility to design new modifiable spintronic devices with logical region sizes limited only by the spatial pattern of the light used for excitation. This will make it possible to investigate new device physics and build new functionalities for skyrmions.

Materials and Methods

1. Methods: Details of the experimental setup

The experiments were carried out in a modified JEOL JEM2100 TEM [35]. In this instrument, *in-situ* cryo-LTEM can be performed in the Fresnel configuration [36] at camera-rate temporal resolution (ms) using a continuous wave electron beam generated thermionically, upon in situ pulsed optical excitation of the specimen with tunable fs source. The camera used for the detection of the electrons was a Gatan® K2 direct detection camera. The sample was cooled to 5K using a helium-cooled sample holder from Gatan.

A Ti:Sapphire regenerative amplifier was used to generate 35-fs pulses of light with a center wavelength at 800 nm and a 34-nm (FWHM) bandwidth. The pulse energy directly from the amplifier was 1.5 mJ per pulse at a 4-kHz repetition rate, and ~55% of this light (0.81 mJ) was used to convert to near-IR wavelength via an optical parametric amplifier (OPA). After conversion to 1200nm/1eV, the pulses have the duration of 50 fs, and we used a series of optical choppers to lower the repetition rate to 10 Hz. In this way, we were able to use a mechanical shutter to send individual pulses as desired, or to send a train of pulses that had a repetition rate lower than the exposure time of our camera. For the pulse train measurements, the pulses had a repetition rate of either 10 Hz or 10 Hz with every 3rd pulse missing (to check for stability). The camera rate was 20 Hz. The absorbed fluence values were computed from the measured FWHM of the beam (30 μ m) using values for the absorption length of the material at this energy from ellipsometry studies in Ref. [37]. The magnetic field in the microscope was applied normal to the sample surface along the [111] direction.

2. Materials: Sample preparation

A high-quality single crystal of Cu_2OSeO_3 was grown by the chemical vapor transport method. 25g of a stoichiometric mixture of CuO and SeO_2 are sealed in a 36mm diameter quartz ampule together with 100mbar of HCl used as transport agent. The ampule is placed in a horizontal two-

zones furnace. During the growth, source and sink temperatures are set at 635°C and 545°C respectively. The single crystal was aligned and cut into a cube so that the three main directions correspond to $[1\bar{1}0]$, $[111]$ and $[\bar{1}\bar{1}2]$, respectively. Then, choosing $[111]$ as the main surface, the cube was cut into slices of ≈ 0.5 mm thickness. The sample was thinned to about 110 nm by Focused Ion Beam (FIB) technique.

Acknowledgements: We acknowledge useful discussions with Achim Rosch, Rofl Versteeg, and Ito Kamier.

Funding: We acknowledge support from the ERC consolidator grant ISCQuM and SNSF via sinergia nanoskymionics grant 171003.

Author contributions:

Conceptualization: PT,BT,AS,FC

Data analysis: BT

Experimental methodology: PT,BT,AS,IM,TL

Investigation: PT,BT,AS

Visualization: PT,BT,AS,TL

Sample preparation: TS,PB,PC,AM

Simulations: SG,PT

Supervision: AM,DG,TL,FC

Writing-original draft: PT

Writing- review and editing: PT,BT,AS,SG,PC,AM,DG,HK,TL,FC

Competing interests: The authors declare no competing interests.

Data and materials availability: All data, code, and materials used in the analyses is available to readers on request.

References:

- [1] A. Fert, N. Reyren, and V. Cros, “Magnetic skyrmions: Advances in physics and potential applications,” *Nat. Rev. Mater.*, vol. 2, 2017.
- [2] K. Litzius *et al.*, “Skyrmion Hall effect revealed by direct time-resolved X-ray microscopy,” *Nat. Phys.*, vol. 13, no. 2, pp. 170–175, 2017.
- [3] W. Jiang *et al.*, “Direct observation of the skyrmion Hall effect,” *Nat. Phys.*, vol. 13, no. 2, pp. 162–169, 2017.
- [4] F. Jonietz *et al.*, “Spin Transfer Torques in MnSi,” *Science (80-.)*, vol. 330, pp. 1648–1652, 2010.
- [5] J. Grollier *et al.*, “Switching a spin valve back and forth by current-induced domain wall motion,” *Appl. Phys. Lett.*, vol. 83, no. 3, pp. 509–511, 2003.
- [6] X. Yu *et al.*, “Real-space observations of 60-nm skyrmion dynamics in an insulating magnet under low heat flow,” *Nat. Commun.*, vol. 12, no. 5079, 2021.
- [7] T. Kampfrath *et al.*, “Terahertz spin current pulses controlled by magnetic heterostructures,” *Nat. Nanotechnol.*, vol. 8, no. 4, pp. 256–260, 2013.
- [8] T. Seifert *et al.*, “Efficient metallic spintronic emitters of ultrabroadband terahertz radiation,” *Nat. Photonics*, vol. 10, no. 7, pp. 483–488, 2016.
- [9] J. Hurst, P.-A. Hervieux, and G. Manfredi, “Spin current generation by ultrafast laser pulses in ferromagnetic nickel films,” *Phys Rev B*, vol. 97, no. 1, p. 014424, 2018.

- [10] A. B. Schmidt *et al.*, “Ultrafast Magnon Generation in an Fe Film on Cu (100),” *Phys. Rev. Lett.*, vol. 105, no. 197401, 2010.
- [11] J. Kimling *et al.*, “Picosecond Spin Seebeck Effect,” *Phys. Rev. Lett.*, vol. 057201, no. 118, 2017.
- [12] A. Alekhin *et al.*, “Femtosecond Spin Current Pulses Generated by the Nonthermal Spin-Dependent Seebeck Effect and Interacting with Ferromagnets in Spin Valves,” *Phys. Rev. Lett.*, vol. 119, no. 1, pp. 1–6, 2017.
- [13] P. Tengdin *et al.*, “Critical behavior within 20 fs drives the out-of-equilibrium laser-induced magnetic phase transition in nickel,” *Sci. Adv.*, vol. 4, no. eaap9744, 2018.
- [14] A. V. Kimel, A. Kirilyuk, P. A. Usachev, R. V. Pisarev, A. M. Balbashov, and T. Rasing, “Ultrafast non-thermal control of magnetization by instantaneous photomagnetic pulses,” *Nature*, vol. 435, no. 7042, pp. 655–657, 2005.
- [15] N. Prasai *et al.*, “Ballistic magnon heat conduction and possible Poiseuille flow in the helimagnetic insulator Cu₂OSeO₃,” *Phys. Rev. B*, vol. 95, no. 22, pp. 1–9, 2017.
- [16] I. Stasinopoulos *et al.*, “Low spin wave damping in the insulating chiral magnet Cu₂OSeO₃,” *Appl. Phys. Lett.*, vol. 111, no. 032408, 2017.
- [17] M. Mochizuki *et al.*, “Thermally driven ratchet motion of a skyrmion microcrystal and topological magnon Hall effect,” *Nat. Mater.*, vol. 13, pp. 241–246, 2014.
- [18] S. Pöllath *et al.*, “Dynamical Defects in Rotating Magnetic Skyrmion Lattices,” *Phys. Rev. Lett.*, vol. 118, no. 20, pp. 1–6, 2017.
- [19] J. S. White *et al.*, “Electric field control of the skyrmion lattice in Cu₂OSeO₃,” *J. Phys. Condens. Matter*, vol. 24, no. 43, 2012.

- [20] J. S. White *et al.*, “Electric-field-induced skyrmion distortion and giant lattice rotation in the magnetoelectric insulator Cu₂OSeO₃,” *Phys. Rev. Lett.*, vol. 113, no. 10, pp. 1–5, 2014.
- [21] M. G. Han *et al.*, “Scaling, rotation, and channeling behavior of helical and skyrmion spin textures in thin films of Te-doped Cu₂OSeO₃,” *Sci. Adv.*, vol. 6, no. 13, pp. 1–9, 2020.
- [22] K. Everschor *et al.*, “Rotating skyrmion lattices by spin torques and field or temperature gradients,” *Phys. Rev. B - Condens. Matter Mater. Phys.*, vol. 86, no. 5, 2012.
- [23] N. Ogawa, S. Seki, and Y. Tokura, “Ultrafast optical excitation of magnetic skyrmions,” *Sci. Rep.*, vol. 5, pp. 1–5, 2015.
- [24] N. Prasai *et al.*, “Spin phases of the helimagnetic insulator Cu₂OSeO₃ probed by magnon heat conduction,” *Phys. Rev. B*, vol. 99, no. 2, pp. 1–5, 2019.
- [25] K. Uchida *et al.*, “Spin Seebeck insulator,” *Nat. Mater.*, vol. 9, no. 11, pp. 894–897, 2010.
- [26] M. Finazzi *et al.*, “Laser-induced magnetic nanostructures with tunable topological properties,” *Phys. Rev. Lett.*, vol. 110, no. 17, pp. 1–5, 2013.
- [27] W. Koshibae and N. Nagaosa, “Creation of skyrmions and antiskyrmions by local heating,” *Nat. Commun.*, vol. 5, 2014.
- [28] J. C. Loudon, A. O. Leonov, A. N. Bogdanov, M. C. Hatnean, and G. Balakrishnan, “Direct observation of attractive skyrmions and skyrmion clusters in the cubic helimagnet Cu₂OSeO₃,” *Phys. Rev. B*, vol. 97, no. 134403, 2018.
- [29] J. Müller *et al.*, “Magnetic Skyrmions and Skyrmion Clusters in the Helical Phase of Cu₂OSeO₃,” *Phys. Rev. Lett.*, vol. 119, no. 13, pp. 1–6, 2017.

- [30] R. B. Versteeg *et al.*, “Optically probed symmetry breaking in the chiral magnet Cu₂OSeO₃,” *Phys Rev B*, vol. 094409, pp. 1–9, 2016.
- [31] S. Mühlbauer *et al.*, “Skyrmion lattice in a chiral magnet,” *Science (80-.)*, vol. 323, no. 6048, pp. 915–919, 2009.
- [32] S. Finizio *et al.*, “Time-resolved visualization of the magnetization canting induced by field-like spin-orbit torques,” *Appl. Phys. Lett.*, vol. 117, no. 21, 2020.
- [33] H. Fujita and M. Sato, “Ultrafast generation of skyrmionic defects with vortex beams: Printing laser profiles on magnets,” *Phys. Rev. B*, vol. 95, no. 5, pp. 1–12, 2017.
- [34] S. Ali, J. R. Davies, and J. T. Mendonca, “Inverse faraday effect with linearly polarized laser pulses,” *Phys. Rev. Lett.*, vol. 105, no. 035001, 2010.
- [35] L. Piazza, D. J. Masiel, T. Lagrange, B. W. Reed, B. Barwick, and F. Carbone, “Design and implementation of a fs-resolved transmission electron microscope based on thermionic gun technology,” *Chem. Phys.*, vol. 423, pp. 79–84, 2013.
- [36] S. McVitie and M. Cushley, “Quantitative Fresnel Lorentz microscopy and the transport of intensity equation,” *Ultramicroscopy*, vol. 106, no. 4–5, pp. 423–431, 2006.
- [37] R. B. Versteeg *et al.*, “Optically probed symmetry breaking in the chiral magnet Cu₂OSeO₃,” *Phys. Rev. B*, vol. 94, no. 9, pp. 1–9, 2016.

Figures:

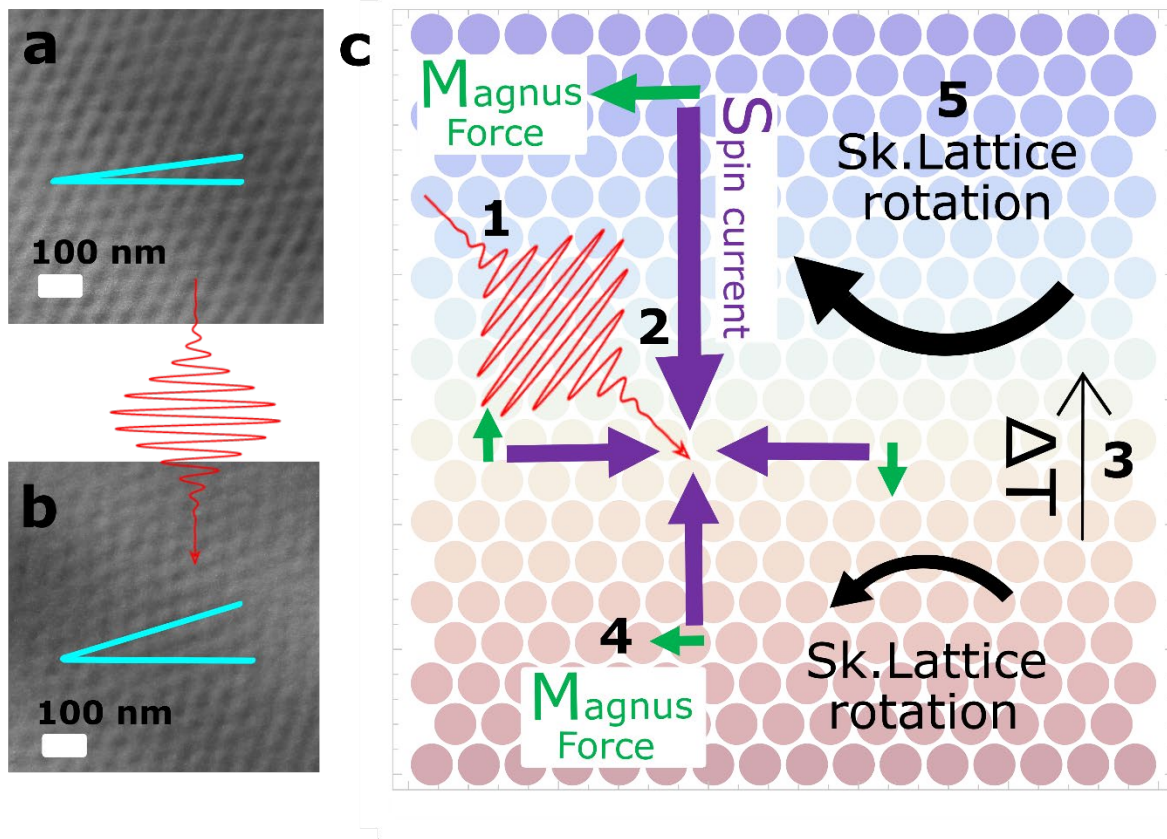


Fig. 1: Illustration and schematic of laser-driven skyrmion crystal rotation process. **a**, Real space image of skyrmion crystal in Cu_2OSeO_3 before excitation with laser pulse. **b**, Image taken after 6 successive near-infrared laser pulses have each rotated the skyrmion crystal by a discrete amount. Note that the angle (depicted in blue) to the horizontal has changed. **c**, Schematic of the mechanism for skyrmion rotation. Dynamics occur in the following manner: 1. Excitation by femtosecond laser pulse. 2. Spin currents excited by the laser will travel in both the forward and backward direction. (items 3-5 occur simultaneously) 3. Shortly after excitation, there exists a thermal gradient (depicted in the blue-red color gradient) that is due to the cooling process and the geometry of our sample. 4. Magnus force occurs due to spin current + gradient 5. The laser generated spin currents, combined with the thermal gradient and the magnus force will induce rotation. The weight of the arrows for the magnus force and spin current in the schematic marks the magnitude.

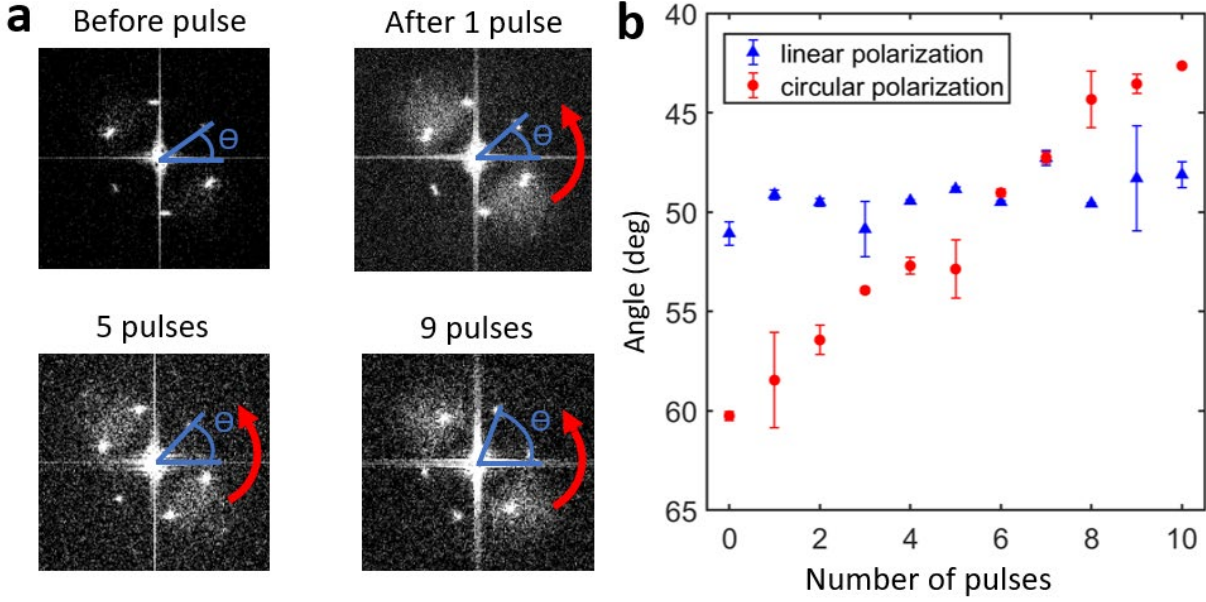


Fig 2. Details of laser-driven skyrmion crystal rotation. **a**, Fourier transforms of L-TEM images following successive pulses of near-infrared femtosecond laser excitation. Note how the angle of the hexagonal ordering of the skyrmion crystal changes as a function of the number of pulses applied to the sample. **b**, Tracking the position of a single peak in the FT of an image while pumping the sample with a train of femtosecond laser pulses. The error bars are 95% confidence intervals calculated from the fit and multiplied by an uncertainty factor determined from the noise level in the data.

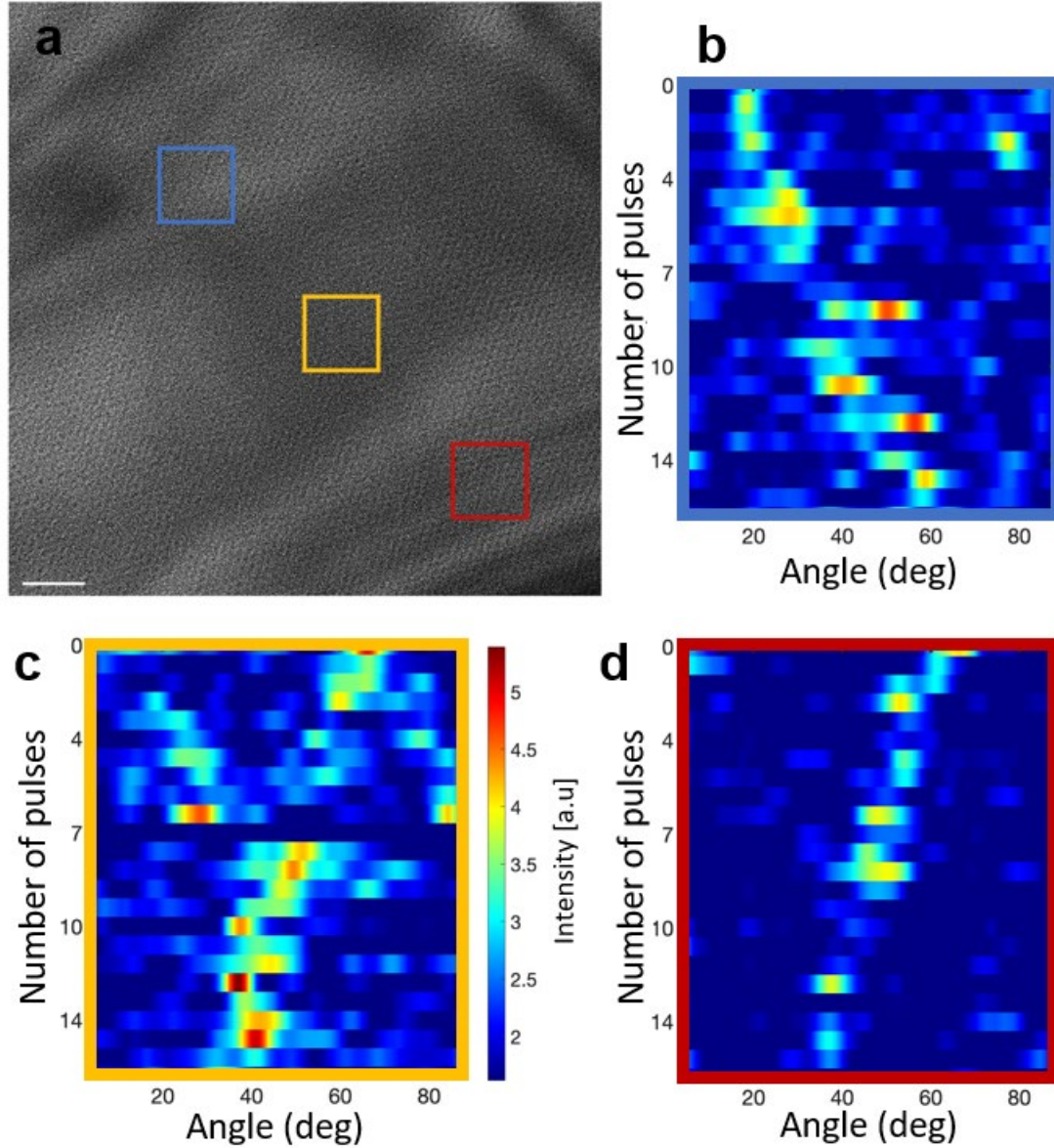


Fig 3. Skymion crystal rotation in a real space image from the TEM. **a**, Real space L-TEM image of the magnetic structure in Cu_2OSeO_3 . Scale bar (bottom left) is 500 nm. Response of the skymion crystal after excitation by a femtosecond laser pulse train is shown for specific regions of the film in **b-d**. We take the FT of each subsection of the image and plot the angle of a single peak in the FT as a function of the number of pulses applied to the sample. The intensity corresponds to the intensity of the peak in the Fourier transform within a region of angles. Note how region **b**, on the upper left hand side of the image displays purely counterclockwise motion while region **d** on the bottom right hand side of the image displays purely clockwise rotation. For the region in the middle, **c** we are looking at a boundary between one domain of skyrmons rotating clockwise and a second domain rotating counter-clockwise. Thus, both rotation senses are present. See SI for rotational maps of the entire film.

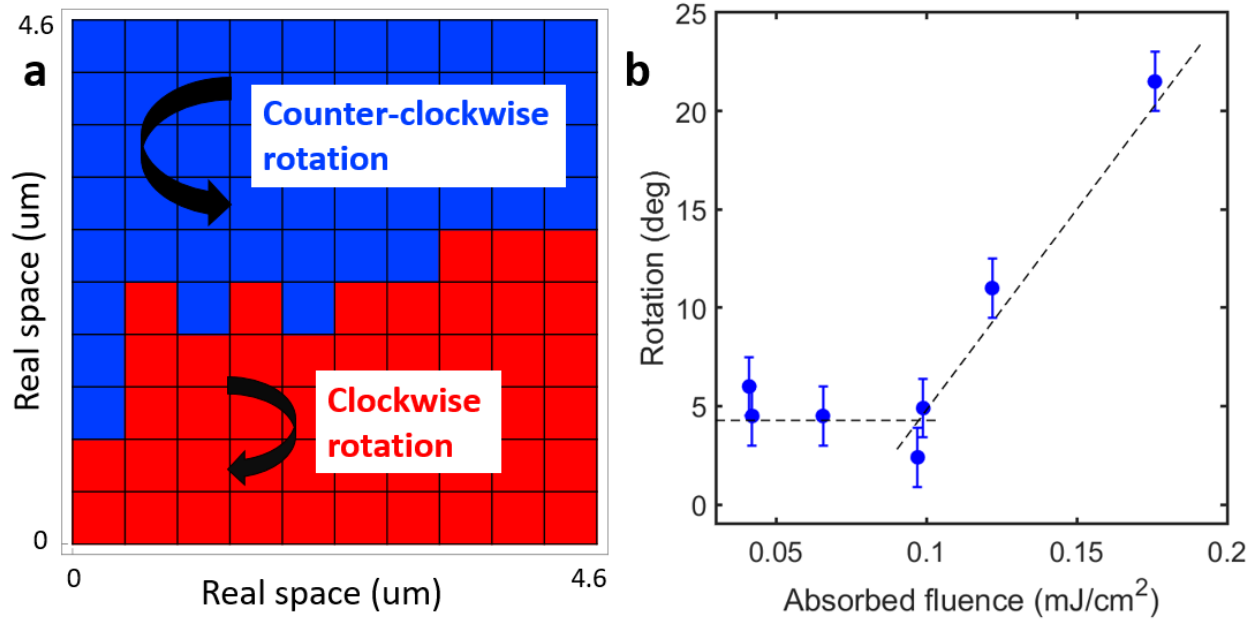


Fig 4. Full field of view of skyrmion crystal rotation and fluence dependence of the rotation. **a**, Real space image of the rotation directions observed in a 10x10 grid of the image from Figure 3b. **b**, Plot of induced rotation angle in the skyrmion crystal as a function of absorbed fluence from the femtosecond laser excitation. Note that above a critical threshold, as the fluence increases, the amount of rotation of the crystal also increases. The error bars are 95% confidence intervals calculated from the fit and multiplied by an uncertainty factor derived from other experimental uncertainties (such as shot-to-shot uncertainty of the laser pulses, etc.)

Supplementary Text:

Contents:

- 1: Details on the gridded analysis of skyrmion rotation in our image
2. Full data of rotation taken from many regions of the lamella with both circular polarization of both handedness and linear polarization
3. Details of the finite element model: final temperature reached following laser pulse excitation
4. Details of the phononic heat capacity and heat conductivity
5. Estimation of sample heating by the electron beam

1: Details on the gridded analysis of skyrmion rotation in our image

The full data set used to generate Figure 4a in the main text is shown in Figure S1 below. The real space image was divided into regions of 460 nm. From each gridded subsection, the Fourier Transform was taken, and a coordinate transform is made from cartesian to polar coordinates. We then integrate over a certain region in the radial coordinate. Due to symmetry, we average the data from angles 0-180° with data from angles 180-360°. We then plot intensity vs. angle and choose the peak with the highest intensity and plot a region in angle space around this peak. This provides us with intensity maps in the angle coordinate as shown in Fig. 3 of the main text. By fitting these intensity maps with a gaussian function, we extract the central peak and use this to plot the function of angle vs. number of pulses seen in Fig. 2 of the main text, and to calculate the fluence dependence for Fig. 4 of the main text.

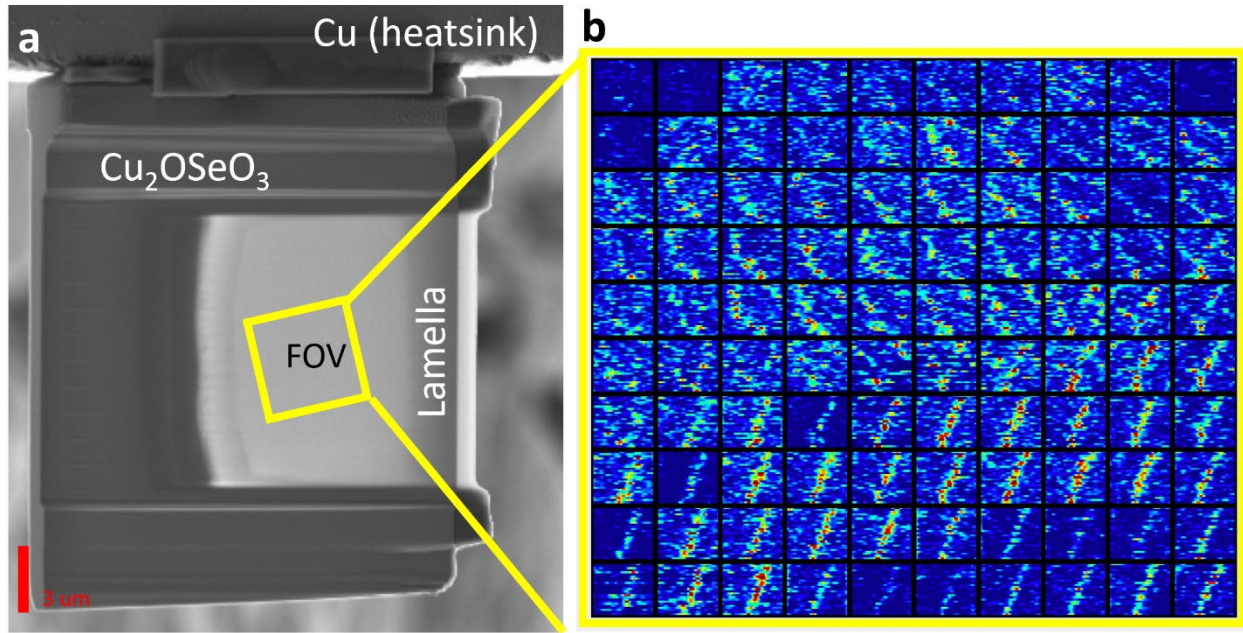


Fig. S1. (a) Scanning electron microscope image of lamella. The scale bar (bottom left) is 3 μm . The range of interest (ROI) of our L-TEM images is given by the yellow box. Note the copper bar marked as heatsink above. This bar determines the thermal gradient that follows the ultrafast heating process. (b) Each box maps the angle of a single point in the FT of a subsection of the image following excitation during a train of circularly polarized laser pulses (1 image for each

pulse). The direction and magnitude of rotation follows a distinct trend, which can be mapped back to the distance of each region of the real space image from the heat sink. The number of pulses sent on the y axis was 16 and the x-axis runs from 3.5 to 88 degrees.

2. Full data of rotation taken from many regions of the lamella with both circular and linear polarization

Additional data was taken with circular and linear polarization in different regions of the film.

The rotation observed in these regions is shown below in Figures S2 and S3. Note that for regions at the top of the film, no rotation is seen for linear polarization (as shown in figure 2b of the main text).

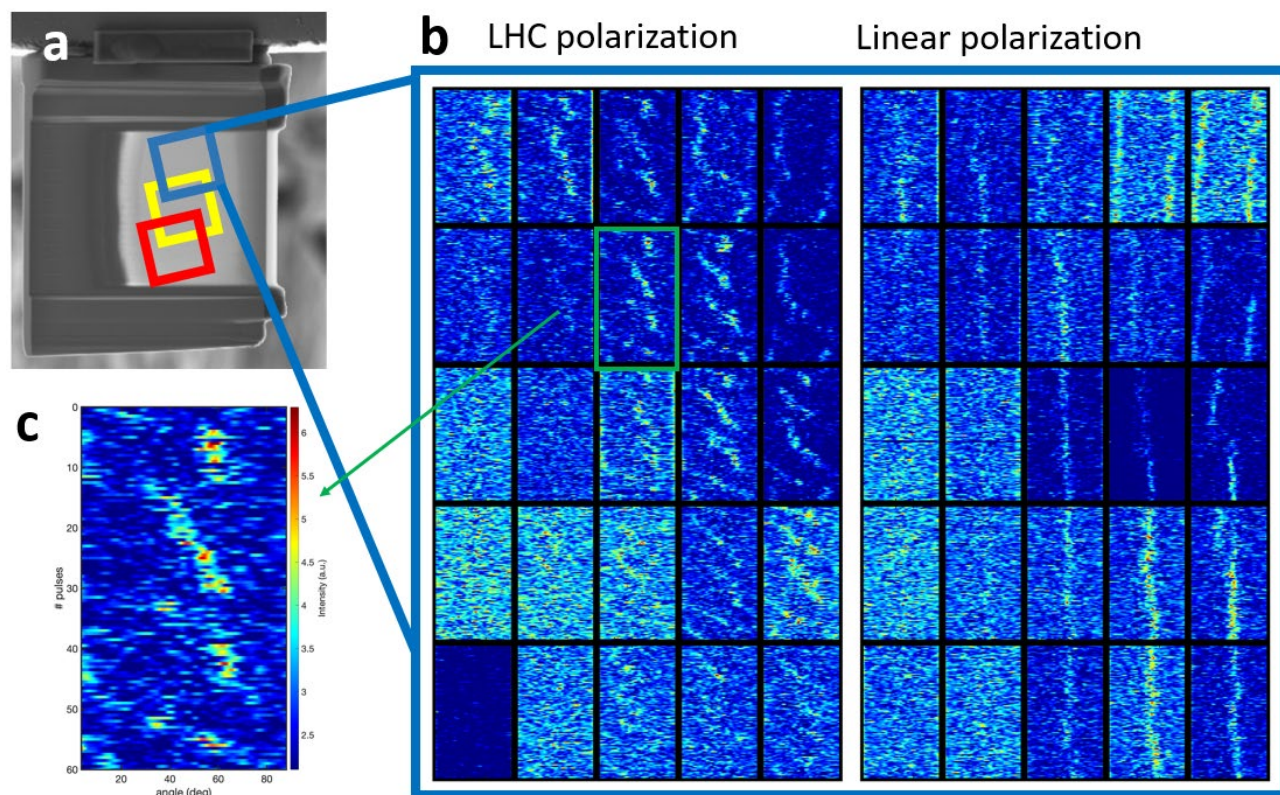


Fig. S2. Data taken with the same methodology as Fig.S1 from a different field of view in the sample using linearly polarized and circular polarization with both handednesses. (a) Shows the region of the sample from which the image was taken approximately and (b) shows the direction

of rotation in a 5x5 grid taken from that region for Left-hand circular, linear, and RHC polarizations. (c) Blow up from a sub-image of (b) shows the axis labels for all subplots shown in part (b).

We note that some regions of the sample have clearly much better signal to noise than other regions. This is because certain regions of the real space image do not have good contrast because of strain induced wrinkles in the film. These wrinkles are called bend contours and are shadows in the TEM image. They can be minimized by tilting the sample, however all samples and all tilt angles have an unavoidable amount of bend contours.

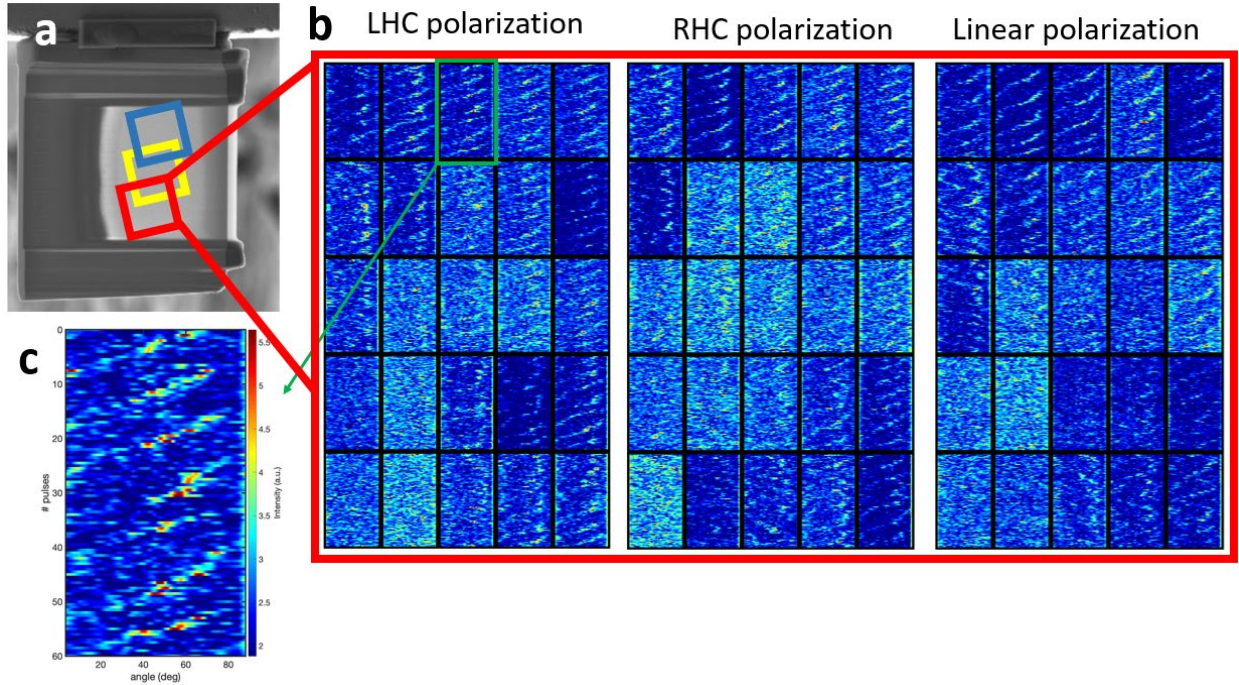


Fig. S3. Data taken with the same methodology as Fig.S1 from a different field of view in the sample using linearly polarized and circular polarization with both handedness'. **a**, shows the region of the sample from which the image was taken approximately and **b**, shows the direction of rotation in a 5x5 grid taken from that region for LHC, linear, and RHC polarizations. **c**, Blow up from a sub-image of (b) shows the axis labels for all subplots shown in part (b).

For the regions far from the copper bar, some rotation is seen for linearly polarized light. We expect this is because these regions will cool off more slowly, giving the spin currents generated by the spin seebeck effect (heat) more opportunity to drive the rotation. linear light can still have a finite (small) circularly polarized component and because it can also drive the inverse Faraday effect via Laguerre gauss modes in the beam[1]. We observe that circularly polarized light rotates the skyrmion crystal more quickly than linearly polarized light in this region.

3. Details of the finite element model: final temperature reached following laser pulse excitation

The thermodynamic finite element model of the Cu_2OSeO_3 sample, heated by an ultrafast laser pulse, has been implemented using *COMSOL*. The geometry implemented is shown in Fig. S2. Here, the domain is divided in two regions: the lamella (in red), with a thickness of 100 nm, and the support (green), with a thickness of 1 μm .

The laser has been described analytically as a Gaussian beam, having a flux $\phi(x, y, t) = T_{opt} \cdot (1 - R) \phi_{inc} \cdot \exp(-2r_f^2/r_s^2) \cdot gp(t, \tau_{pulse})$, with a spot radius of $r_s = 20 \mu\text{m}$ and incident from the top with a power density $\phi_{inc} = 3.10 \times 10^{11} \text{ W/cm}^2$ (corresponding to the incident fluence of 15.5 mJ/cm^2 , absorbed fluence value of 0.09 mJ/cm^2). r_c is the radial distance from the beam axial center and is defined as $r_c^2 = (x - x_c)^2 + (y - y_c)^2$, with x_c and y_c being the planar coordinates of the central axis. $T_{opt} = 0.88$ is the transmission coefficient of the optical system (window and reflective mirror inside the microscope) while $R = 0.11$ is the reflection coefficient of Cu_2OSeO_3 at $\lambda = 1.24 \mu\text{m}$ (1 eV). $gp(t, \tau_{pulse})$ is a normalized gaussian pulse with duration $\tau_{pulse} = 50 \text{ fs}$ and centered around $t_i = 0.5 \text{ ps}$. The heating induced on the sample by

the laser pulse has been introduced through a volumetric heat source, modelled as $Q_0 = \alpha \phi_{inc} \exp(\alpha(z - z_0))$, where $\alpha = 318.66 \text{ cm}^{-1}$. Here, z_0 corresponds to the longitudinal coordinate of the top surfaces for both lamella and support. One of the support's lateral surfaces has been fixed to the temperature of 5K, emulating the behavior of the heatsink. Initial temperature has been set to 5K all over the structure.

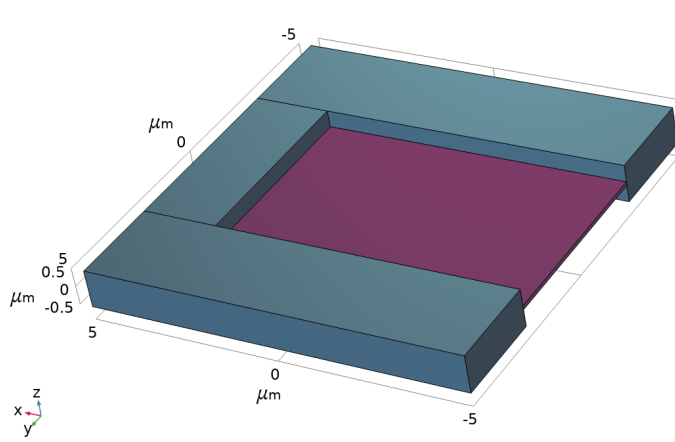


Fig. S2. Geometry of the Cu₂OSeO₃ sample implemented in Comsol Multiphysics. The domain has been divided in two regions: the lamella in purple and the support in gray.

The time dependent simulation is run for a period of $1.4 \mu\text{s}$, considering the temperature dependent heat capacity $C(T)$ and heat conductivity $k_L(T)$ discussed in Section 4, with non-uniform time steps.

The temperature trend resulting from the simulation are shown in Fig. S3. Here, we show the maximum, minimum and average temperatures reached by the sample as a whole (Fig. S3A) and by the lamella (Fig. S3B) following the laser excitation. Fig. S3A shows that the absolute maximum temperature reached by the support is $\sim 48.5 \text{ K}$ at $t_m = 0.660 \text{ ps}$, meaning that it is delayed with respect to t_i (and the center of the excitation pulse) by about 160 fs. The average temperature slowly decays to $\text{avg}(T) \sim 40 \text{ K}$ reached in $t \sim 40 \text{ ns}$ and finally to 5K in a time

interval of $1.3 \mu s$. Maximum temperature in the support is kept almost constant up to $t \sim 250 ns$, corresponding to the onset of the cooling of the last part of the support, the farthest from the heatsink. The minimum temperature measured all over the support is always 5K, representative of the heatsink surface. Fig. S3B shows that the absolute maximum temperature reached by the thin lamella is of $\sim 49 K$ for $t = t_m = 0.660 ps$. The temperature in the lamella is quite uniform during the heating phase, in fact $\max(T) - \min(T) = 2$ or $3 K$. At $t \sim 15 ns$ the minimum temperature drops from $\sim 46K$ to $\sim 12K$ in $25 ns$, meaning that the cold region, with the temperature imposed by the heatsink, is entering the lamella's domain.

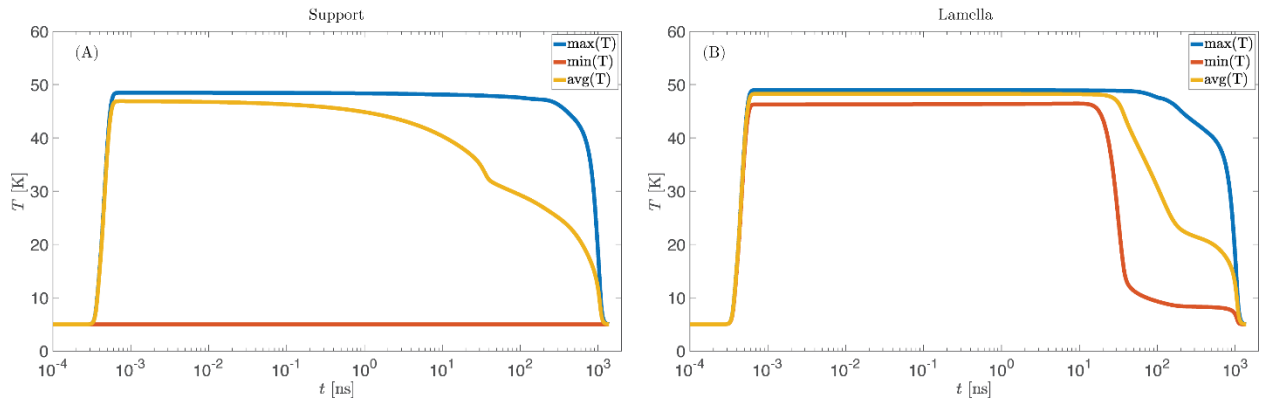


Fig. S3. Maximum (blue), minimum (red) and average (yellow) temperature obtained in the support (A) and in the lamella (B).

The entire process of cooling takes approximately $1.3 \mu s$.

Fig. S4 shows the isothermal contours obtained on the top surface at $t \sim 15 ps$. The gradient imprinted on the surface is circular due to the gaussian shape of the laser beam. Note that within the region of the lamella (where measurements are taken), the heating is nearly uniform (gradient less than 1 K over 10 μm).

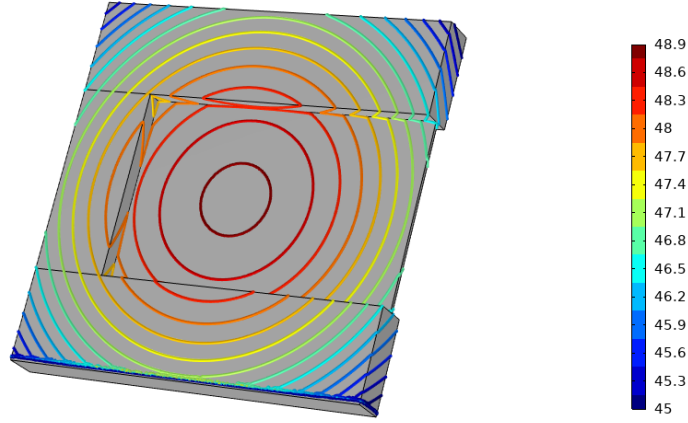


Fig. S4. Isothermal contours after laser irradiation ($t=15$ ps) on the top surface. White labels represent the temperature. Heat sink surface is on the bottom left.

Fig. S5 shows the temperature map at $t \sim 125$ ns, thus during the cooling process of the lamella. Here the temperature gradient between the hot and cold regions is much more pronounced than the one obtained during the heating process (as highlighted in Fig. S4). The gradient, during this phase, is imprinted by the heatsink, leading to a linear boundary between the hot and cold domains.

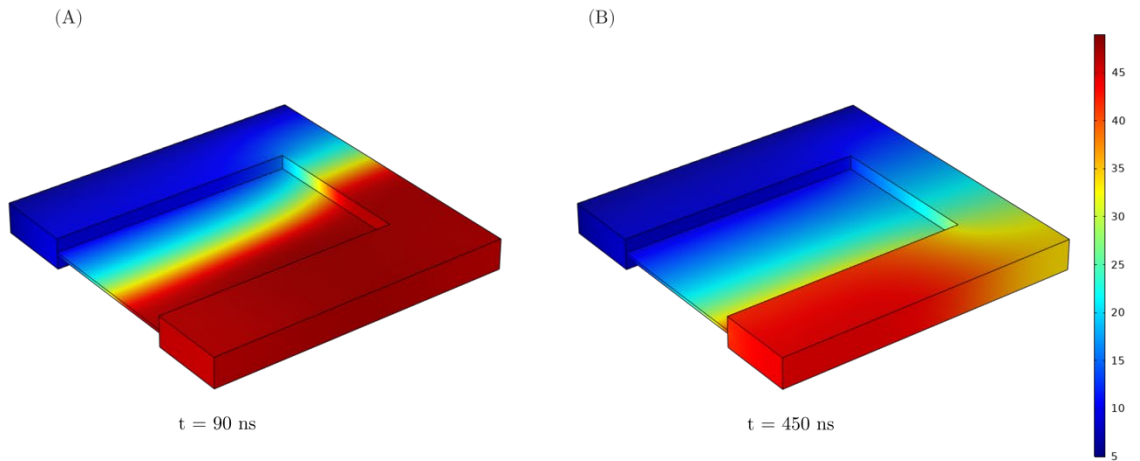


Fig. S5. Temperature map of the Cu_2OSeO_3 sample during the cooling phase in two different time instants: at $t = 90$ ns (A) and $t = 450$ ns (B). Color legend indicates the temperature in Kelvin.

The top left surface is representative of the heat sink and it is kept at the constant temperature of 5K during the simulation.

4. Details of the phononic heat capacity and heat conductivity

Experimental data on the temperature dependent heat capacity of Cu_2OSeO_3 has been retrieved from Ref. [2].

For the heat conductivity we used the Callaway model [3], together with its update [4], as done in Ref. [5]. In particular, the integral expression for the phononic heat conductivity is the following:

$$k_L = \frac{k_B}{2\pi^2 v} \left(\frac{k_B}{\hbar} \right)^3 T^3 \left[\int_0^{\theta_D/T} \frac{x^4 e^x}{(e^x - 1)^2} \tau_c(x, T) dx \right] \times \left(1 + \frac{\overline{\tau_c(T)/\tau_N(T)}}{\overline{\tau_c(T)/\tau_R(T)}} \right) \quad (1)$$

with

$$\frac{\overline{\tau_c(T)/\tau_N(T)}}{\overline{\tau_c(T)/\tau_R(T)}} = \int_0^{\theta_D/T} \frac{x^4 e^x}{(e^x - 1)^2} \frac{\tau_c(x, T)}{\tau_N(x, T)} dx \bigg/ \int_0^{\theta_D/T} \frac{x^4 e^x}{(e^x - 1)^2} \frac{\tau_c(x, T)}{\tau_R(x, T)} dx \quad (2)$$

where v is the Debye-averaged sound speed, $x = \hbar\omega/k_B T$ is the reduced phonon energy and $\tau_c^{-1}(x, T) = \tau_N^{-1}(x, T) + \tau_R^{-1}(x, T)$. In the latter equation $\tau_N^{-1}(x, T)$ and $\tau_R^{-1}(x, T)$ are the phonon scattering rates for the normal (that conserve momentum) and resistive processes (that do not conserve the momentum), respectively. Their expressions are given below:

$$\tau_R^{-1}(x, T) = v/l_{ph} + A x^2 T^4 \exp\left(-\frac{\theta_D}{b T}\right) + C x^4 T^4 \quad (3)$$

$$\tau_N^{-1}(x, T) = \gamma A x^2 T^4 \quad (4)$$

$\tau_R^{-1}(x, T)$ includes terms accounting for scattering from boundaries (Umklapp scattering), other phonons and point-like defects. Here A , b , C and γ are fitting parameters. To model our 10 μm Cu_2OSeO_3 sample, we used for A, b, C and γ the values reported in Ref. [5] for the smallest

available specimen ($l_0 = 0.15 \text{ mm}$), reevaluating k_L assuming $l_{ph} = l_0 = 10 \text{ um}$. Fig. S5 reports the heat conductivity obtained following the aforementioned model. More precisely the fitting parameters used are: $v = 2.35 \text{ km/s}$, $A = 1.5 \times 10^4 \text{ K}^{-4}$, $b = 6.35$, $C = 110 \text{ K}^{-4}$, and $\gamma = 0$. The condition $\gamma = 0$ is equivalent to setting $\frac{\tau_c(T)/\tau_N(T)}{\tau_c(T)/\tau_R(T)} = 1$.

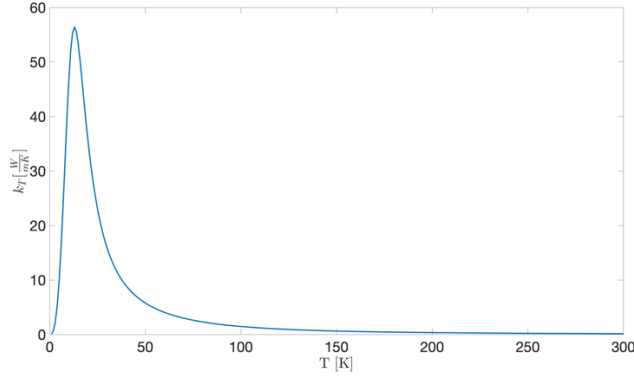


Fig S5. Analytical heat conductivity obtained with the Callaway model using the fitting parameters of Ref. [13] and $l_{ph} = l_0 = 10 \text{ um}$.

5. Estimation of sample heating by the electron beam

We affirmatively state that absolutely no rotation of the skyrmion crystal was observed in our microscope without the application of the laser pulses. Experimentally, we have observed the metastable skyrmion crystal under the conditions of 5K, 34mT applied field, and confirmed that there is no rotation present on the timescale of 10 minutes.

Sample heating from the electron beam is intrinsic to TEM measurement, although the amount of heating varies widely and depends on the sample and imaging conditions—heating results from inelastic scattering processing from interactions with high energy and sample electrons. The high-energy electrons lose energy and transfer an appreciable amount of energy to the sample. Most of this energy generates plasmons and lattice phonons in the sample, giving a higher local temperature rise than the temperature of the surroundings. We estimate the temperature rise in Lorentz TEM experiments by implementing the expression of Egerton et al. for beam heating resulting from inelastic scattering[6].

$$I\langle E(eV)\rangle(t/\lambda) = \frac{4\pi\kappa t(T - T_0)}{\left[0.58 + 2\ln\left(\frac{2R_0}{d}\right)\right]} + \pi\left(\frac{d^2}{2}\right)\varepsilon\sigma(T^4 - T_0^4) \quad (6)$$

This simplified model equates the inelastic loss energy deposited and heats the sample to the conductive and radiative losses in a thin TEM specimen. $\langle E \rangle$ corresponds to the average energy loss per collision, and the average energy *per incident electron* is $\langle E \rangle (t/\lambda)$, where t is thickness and λ is the mean free path for all inelastic scattering. The heat deposited in the specimen per second (in units of eV) is $(I/e) \langle E \rangle (t/\lambda)$, where I is the beam current and e is the electronic charge. The steady-state beam heating from an incident beam current I with a diameter d equilibrates with heat loss due to radial conduction (over a distance R_0 through the material of thermal conductivity κ) and radiative losses (from both surfaces of the specimen, emissivity ε). However, radiative losses are typically negligible due to the slight temperature rise associated with electron beam heating, but we included it for completeness of the analysis

Putting numbers from the LTEM imaging experiments into Equation (6):

An average energy loss and deposited energy $\langle E \rangle = 20\text{eV}$

Electron beam diameter (d) = 5 μm

The estimated beam current $I = 15\text{nA}$

The inelastic mean free path was calculated from Malis et al $\lambda = 76.5\text{ nm}$

(Malis et al., J. Electron Microsc. Tech. vol. 8 (1988) p193)

The thermal conductivity was taken from reference Prasai et al., $\kappa = 170\text{ W/m-K}$

(Prasai, N., et al., Ballistic magnon heat conduction and possible Poiseuille flow in the helimagnetic insulator Cu_2OSeO_3 . Physical Review B, 2017. 95(22): p. 224407)

The estimated sample thickness $t = 100\text{nm}$

The emissivity $\varepsilon = 0.35$

The maximum radial conduction length to the heat sink $R_0 = 5\text{ }\mu\text{m}$

The temperature rise due to beam heating in these experiments is quite small, $\Delta T = T - T_o = 5\text{mK}$.

While beam heating is known to induce phase transitions and even melt samples, the temperature rises are inherently small due to the illumination conditions required for the LTEM. The moderate condenser apertures and spread beam (5 μm diameter) provide the improved coherence necessary for imaging skyrmions with the LTEM phase contrast imaging technique in our thermionic TEM. Furthermore, we can reduce the dose to 10 electrons/ nm^2 using Gatan® K2 direct detection camera, which are comparable to cryoBio-TEM experiments for imaging sensitive protein molecules. At such low electron dose, we also limit radiation damage and other effects, e.g., sample charging and electrical field induced motion.

References:

- [1] S. Ali, J. R. Davies, and J. T. Mendonca, “Inverse faraday effect with linearly polarized laser pulses,” *Phys. Rev. Lett.*, vol. 105, no. 035001, 2010.
- [2] T. Adams *et al.*, “Long-wavelength helimagnetic order and skyrmion lattice phase in Cu₂OSeO₃,” *Phys. Rev. Lett.*, vol. 108, no. 23, pp. 1–5, 2012.
- [3] R. Berman, *Thermal Conduction in Solids*. Oxford Press, 1976.
- [4] P. B. Allen, “Improved Callaway model for lattice thermal conductivity,” *Phys. Rev. B - Condens. Matter Mater. Phys.*, vol. 88, no. 14, pp. 1–5, 2013.
- [5] N. Prasai *et al.*, “Ballistic magnon heat conduction and possible Poiseuille flow in the helimagnetic insulator Cu₂OSeO₃,” *Phys. Rev. B*, vol. 95, no. 22, pp. 1–9, 2017.
- [6] R. F. Egerton, P. Li, and M. Malac, “Radiation damage in the TEM and SEM,” *Micron*, vol. 35, no. 6, pp. 399–409, 2004.